Preference-Based Multiobjective Optimization of Nonresonant Wireless Charging System

Hao Liu, Zhenjie Li, *Member, IEEE*, and Henglin Chen

***Abstract*—Desensitizing the misalignment and achieving low loss can improve the performance of wireless charging systems (WCS). A preference-based multiobjective optimization and resistance estimation algorithm based on the orthogonal table and multiple linear regression is used to achieve this. First, the working principle of a nonresonant WCS is analyzed to illustrate the relationship between WCS performance and mutual inductance along with coil resistance. Then, based on the orthogonal method and F-test, the parameters affecting the coil resistance are determined, and an estimation model for the coil resistance is established. Third, preference region and Latin hypercube sampling (LHS) are added to the nondominated sorting genetic algorithm II (NSGAII) method to enhance individual density within the preferred region without increasing the number of individuals and optimize the antimisalignment ability and coil resistance based on the model above of nested coils as an example using the proposed method. Compared to the NSGAII method, the mutual inductance fluctuation within 120 mm is reduced by 58% under similar conditions. Finally, the simulation and experimental results demonstrate that the proposed resistance estimation method has acceptable accuracy, and the proposed optimization method can optimize the horizontal antimisalignment ability of nested coils, and thus constant voltage/constant current charging is achieved.**

***Index Terms*—Orthogonal method, preference-based multiobjective optimization, resistance estimation, target region-based NSGAII (T-NSGAII), wireless charging system (WCS).**

I. INTRODUCTION

WIRELESS power transfer [wireless charging system (WCS)] is a widely used technology and is applied in many fields, such as the charging of electric vehicles, drones, and robots [1], [2], [3]. Meanwhile, power transfer efficiency has become a concern. The efficiency of inverters, loss of magnetic coupling structure, and rectifiers mainly determine power transfer efficiency. As the efficiency of rectifiers and inverters is determined more by the performance of semiconductor devices, this article mainly focuses on the loss of coils, which can be optimized by coupling coil design.

As coupling structures always have many parameters and finite element analysis (FEA) is time-consuming, the exhaustive method may spend too much time and computing resources. So, optimization methods are used to find parameter combinations that meet the requirements in a shorter time. Mathematical modeling proved to be a powerful way to optimize the coils [4]. This method establishes mathematical models of magnetic coupling structure and uses mathematical methods to optimize. Considering that in some cases, the established mathematical models are complex, and methods such as particle swarm optimization (PSO) [5], genetic algorithm (GA) [6], and distance-based-intelligent PSO [7] were used to deal with these cases. Also, identifying the parameters of WCSs can use these methods [8], [9]. However, establishing mathematical models is difficult if the magnetic coupling structure is complex. In [10], a model-free optimization, or black-box optimization based on balanced particle swarm optimization, was established to improve the antimisalignment ability of laminated magnetic coupler. This type of method uses FEA combined with mathematical models to evaluate the performance of magnetic coupling structures. It uses optimization methods such as (PSO) [11] and Tabu search [12] to achieve the optimized goal.

There is not always only one performance indicator for evaluating magnetic coupling structures. This situation requires multiobjective optimization methods. In [13], exhaustive methods and mathematical modeling optimized efficiency, isolation capacitance, and E-field. Similarly, the exhaustive method still has the drawback of extensive time and computing resource costs. So, a weight-based multiobjective optimization algorithm was used to convert multiobjective optimization to single-objective optimization [14]. However, this method can only find one tradeoff between multiple objectives, which may not meet the requirements. Pareto front-based multiobjective optimization methods, such as nondominated sorting genetic algorithm II (NSGAII), were used to find a balance between multiple objectives [15]. Moreover, multiobjective particle swarm optimization (MOPSO) [16] was used to achieve multiobjective optimization of WPT. In addition, MOPSO may be more complex because it is hard to determine the particles to follow.

However, as the number of optimization goals increases, the density of individuals on the Pareto front decreases sharply. The slow FEA makes it difficult for many individuals to use, further exacerbating the problem above. The preference-based multiobjective optimization algorithm solved this problem to a

---

Manuscript received 8 February 2024; revised 21 May 2024; accepted 15 June 2024. Date of publication 20 June 2024; date of current version 4 September 2024. This work was supported in part by the National Natural Science Foundation of China under Grant 52107001. Recommended for publication by Associate Editor J. Acero. *(Corresponding author: Henglin Chen.)*

Hao Liu and Henglin Chen are with the College of Electrical Engineering, Zhejiang University, Hangzhou 310027, China (e-mail: liu.hao@zju.edu.cn; henglin@zju.edu.cn).

Zhenjie Li is with the College of Computer and Control Engineering, Northeast Forestry University, Harbin 150040, China (e-mail: lizhenjie0725@nefu.edu.cn).

Color versions of one or more figures in this article are available at https://doi.org/10.1109/TPEL.2024.3416993.

Digital Object Identifier 10.1109/TPEL.2024.3416993

certain extent by using reference points [17], preference regions [18], reference directions [19], and other methods to bring individuals closer to decision-maker preferences. However, for multiobjective optimization of WCS, preference may be more like a preferred region, such as the range of mutual inductance. So, this article uses a preference regions-based multiobjective optimization algorithm to optimize WCS. Some preferential multiobjective optimization algorithms were proposed and used to maximize satellite mission arrangements [20]. These methods use preferences as one of the sorting criteria to cause individuals to gather in the preferred region, and they use shared distance and hypervolume contribution to make individuals gather near the preferred region when the preferred region does not include the Pareto front. However, the optimization algorithm applied to WCS should be simple and have good convergence due to the problematic modeling and slow FEA calculation. So, target region-based NSGAII (T-NSGAII) is used to optimize WCS in this article, and Latin hypercube sampling (LHS) is used to determine the initial value of the algorithm.

As for the magnetic coupling structure loss estimation, coil resistance is an important factor [21]. So far, methods to estimate coil resistance and loss can be roughly divided into two categories. First, it is the method of combining empirical formulas or physical models with experiments. Empirical formulas [22] or physical models [23] are roughly used to calculate the coil resistance. Then, experiments were set up to correct model errors. Second, the method based on FEA and experiments mainly uses FEA software to calculate coil resistance or loss [12]. Also, these methods can estimate ferrite loss [24], [25], [26]. Although FEA-based methods are more accurate when the input of all factors is accurate, it may take more time, and factors may not be easy to determine. At the same time, empirical formulas or physical models may have errors that need lots of experiments to correct, which also costs time. Taguchi method (TM) has the advantages of uniform dispersion, neatness, and comparability and is widely used in experimental research [27]. Considering that the size, number of turns, shape, and distribution of magnetic cores of the coil may all be parameters that affect the losses of magnetic coupling structures, the TM combined with multiple linear fitting is used in this article to estimate the resistance of the magnetic coupling structure and to estimation the losses of magnetic coupling structure.

The main contributions of this article are given as follows.

1) A magnetic coupler resistance estimation method is proposed based on the orthogonal table and multiple linear regression. Unrelated variables are excluded based on the F-test, and a mathematical model of magnetic coupler resistance is derived. The accuracy of resistance estimation is validated, and the loss of the magnetic coupler is estimated based on the derived model. Then, experimental verification is used to verify its applicability further, and the results show that the average error of the proposed resistance estimation method is about 5%.
2) Preference-based multiobjective optimization, which can increase individual density within the preferred region without increasing the number of individuals, is used to optimize the resistance and antimisalignment ability of the magnetic coupling structure. The principle of the optimization method is analyzed, and optimization of nested coil based on the resistance estimation above is an example of the proposed method. The result shows that the antimisalignment ability and the resistance of the coil are optimized, and higher antimisalignment ability and higher efficiency are achieved compared with the result of the traditional NSGAII method. The experiment verified its ability to resist misalignment and achieved CC/CV charging.

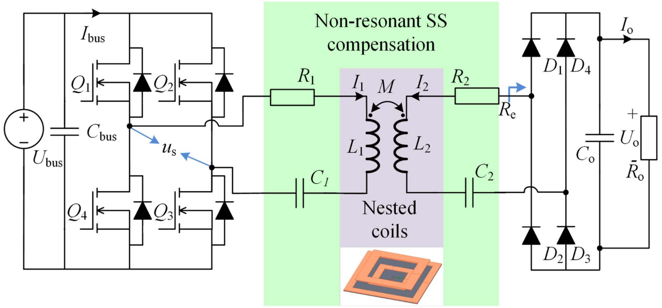

Fig. 1. WCS with nonresonant SS compensation.

The rest of the article is organized as follows. Section II analyzed the antimisalignment ability and loss of the WCS with nonresonant SS compensation. Section III analyzes the loss estimation model of magnetic coupling structure based on the orthogonal method. Section IV analyzes the proposed preference-based multiobjective optimization method and uses the above algorithm to optimize the design of nested coils. Section V verifies the optimized magnetic coupling structure with the experimental results. Finally, Section VI concludes this article.

II. ANTIMISALIGNMENT AND LOSS ANALYSIS OF NONRESONANT WCS

The circuit of the WCS with nonresonant SS compensation is shown in Fig. 1. At the transmitter side, the full-bridge inverter of the system is composed of four MOSFETs (Q_1–Q_4). The resonant capacitor (C_1) is set not to fully compensate for the inductance of the transmitter coil (L_1). At the receiver side, the resonant capacitor (C_2) is set to fully compensate the inductance of the receiver coil (L_2), a full-bridge rectifier including four diodes (D_1–D_4) is used for rectification, and the capacitive filter (C_o) is used to stabilize the output voltage. Mutual inductance between L_1 and L_2 is M. U_{bus} is the system's input voltage, and U_s refers to the inverter's output voltage. The resonant current flows through L_1 and L_2 are I_1 and I_2, respectively, while R_1 and R_2 refer to the transmitter and receiver coil resistance, respectively. The system output voltage is U_o, and the equivalent load resistance is R_o. The rectifier and load are considered resistors (R_e) to simplify the analysis.

Because the circuit with a nonresonant transmitter and the resonant receiver performs better, inductive nonresonant can reduce the risk of MOSFET damage [28]. The circuit parameters

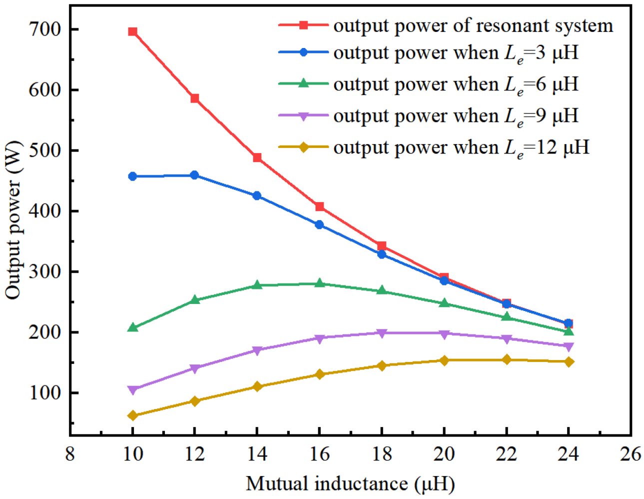

Fig. 2. Output power versus mutual inductance of WCS in different resonant conditions.

of the WCS need to satisfy the following equation:

$$\frac{1}{j\omega C_1}+j\omega(L_1-L_e)=0$$
$$\frac{1}{j\omega C_2}+j\omega L_2=0. \tag{1}$$

In (1), L_e refers to the remaining inductance after compensation. So, the output current can be given by

$$I_2=\frac{j\omega MU_s}{\omega^2M^2+j\omega L_e(R_2+\mathrm{R_e})+R_1R_2+R_1\mathrm{R_e}}. \tag{2}$$

The current flowing through the transmitter coil can be given by (3), and the output power can be given by (4).

$$I_1=\frac{U_s(R_2+\mathrm{R_e})}{(j\omega L_e+R_1)(R_2+\mathrm{R_e})+\omega^2M^2} \tag{3}$$

$$P_o=\mathrm{Re}\left(\frac{j\omega MU_s}{\omega^2M^2+j\omega L_e(R_2+R_e)+R_1R_2+R_1R_e}\right)^2R_e. \tag{4}$$

According to (2) and (3), the loss power of the coils can be given by (5) and (6). The total loss of power is the sum of the two above. In other words, it is P_1+P_2.

$$P_1=\mathrm{Re}\left(\frac{U_s(R_2+\mathrm{R_e})}{(j\omega L_e+R_1)(R_2+\mathrm{R_e})+\omega^2M^2}\right)^2R_1 \tag{5}$$

$$P_2=\mathrm{Re}\left(\frac{j\omega MU_s}{\omega^2M^2+j\omega L_e(R_2+\mathrm{R_e})+R_1R_2+R_1\mathrm{R_e}}\right)^2R_2. \tag{6}$$

According to (4), the output characteristic of the nonresonant SS compensation WCS is neither constant current nor constant voltage. However, the system's antimisalignment ability is enhanced.

As shown in Fig. 2, a WCS with 50 V of U_{bus} and 25 Ω of R_o is taken as an example. When mutual induce fluctuates when misalignment occurs, the output power of the resonant system fluctuates sharply, while the output power of the nonresonant system does not fluctuate so much. However, the efficiency of the nonresonant system drops due to the increasing current of i_1. So, the antimisalignment ability of the nonresonant system is clarified. The L_e is set at 6 μH to balance the antimisalignment ability and output power, and the corresponding mutual inductance interval is 12–24 μH.

As shown in (2) and (3), the short-circuit current and the current when the receiver is open-circuit are limited. So, open-circuit and short-circuit protection is achieved. The whole loss of the WCS is related to R_1 and R_2, as shown in (5) and (6). So, the coil resistance estimation and optimization are necessary for improving system efficiency, which is analyzed in Sections III and IV. Also, the nested coil is chosen for the magnetic coupler to improve antimisalignment ability and reduce coil resistance.

III. TAGUCHI-BASED COIL RESISTANCE AND LOSS ESTIMATION

A mathematical model of magnetic coupling structure based on physical models is challenging to propose due to the ferrite core's uneven magnetic field and the coil's complex design. So, coil resistance and loss estimation based on the TM can simplify the modeling process, and the coil loss is also estimated. The principle of this method is analyzed in the following section.

A. *Analysis of Taguchi Method*

TM is a widely used method developed by Genichi Taguchi for optimizing and modeling processes. This method uses orthogonal tables, which can be obtained by some algorithms to achieve uniform and dispersed sampling and avoid the extensive experimentation required for an exhaustive method. The process of using the orthogonal method for resistance estimation is as follows.

1) Divide parameters into several levels.
2) Find an appropriate orthogonal table based on the number of levels and make necessary modifications to couple the number of parameters and levels of the orthogonal table.
3) Experiment on all combinations in the orthogonal table and collect data.
4) Use the F-test to determine which independent variables impact the dependent variable.
5) Multiple linear regression estimates the relationship between variables.

After obtaining the experimental data combined in the orthogonal table, this article uses the least squares method for linear fitting. The model of multiple regression follows

$$y=\beta_0+\sum_{i=1}^{n}\beta_ix_i \tag{7}$$

where i refers to the number of independent variables and β refers to the coefficients of each independent variable. The following equation is used to calculate β:

$$\beta_i=\sum(x_i-\overline{x_i})(y_i-\overline{y})\Big/\sum(x_i-\overline{x_i})^2 \tag{8}$$

TABLE I
DIFFERENT LEVELS OF PARAMETERS

level	shape	size	Number of turns	Ferrite cores distribution
1	circular	150mm	5	No ferrite core
2	square	210mm	10	Half ferrite core
3	rectangle	300mm	15	Full ferrite core

TABLE II
PARAMETER COMBINATIONS OF THE $L_9 3^4$ ORTHOGONAL TABLE

Experiment no.	turns	size	shape	cores distribution
1	5	150mm	circular	No ferrite core
2	5	300mm	square	Half ferrite core
3	5	210mm	rectangle	Full ferrite core
4	10	300mm	circular	Full ferrite core
5	10	210mm	square	No ferrite core
6	10	150mm	rectangle	Half ferrite core
7	15	210mm	circular	Half ferrite core
8	15	150mm	square	Full ferrite core
9	15	300mm	rectangle	No ferrite core

where x_i refers to each independent variable, y_i refers to the dependent variable, and in this case, it refers to the measured resistance.

B. Establishment of Coil Resistance Model

Coils usually have different shapes, sizes, and turns, and the distribution of their ferrite cores also varies. So, all the aforementioned should be considered. The number of variables is four. The ($L_9 3^4$) orthogonal table, which can accommodate four factors with only nine experimental runs, is selected.

Before experimenting, the parameters in the orthogonal table need to correspond to the actual parameters. As mentioned above, shape, size, number of turns, and ferrite core distribution are used as variables for analysis. The level division method of these variables is given in Table I.

Three typical shapes are selected to be analyzed, and the coil size is also selected as the parameter to be analyzed to consider the influence of coil size. The size of the rectangle coil represents the length of the long side of the coil, where the length of the short side is half of the length of the long side. For circular-shaped and square-shaped coils, parameter size represents the side length and diameter length, respectively.

The number of turns is selected as a parameter to simulate the effect of different turns on the resistance of coils, and ferrite core distribution is also selected because the distribution of coil ferrite cores is different. Among them, the full ferrite core represents the ferrite core covers the whole area below the coil, half ferrite core represents half of the ferrite core is used and distributed as evenly as possible below the coil, and no ferrite core represents the coil does not have a ferrite core beneath it.

The orthogonal table after using the parameters is given in Table II.

The coils in the table above are made, and their resistance was measured using a VC4092E LCR meter at 85 KHz. The main parameters of the coils are given in Table III, and the shape of the coil is shown in Fig. 3.

TABLE III
MAIN PARAMETERS OF THE COILS

Parameter	Value
Model of Litz wire	0.05 mm*1200
Equivalent cross-sectional area	1.96 mm2
Model and size of ferrite core	PC95, 53*53*2.5 mm

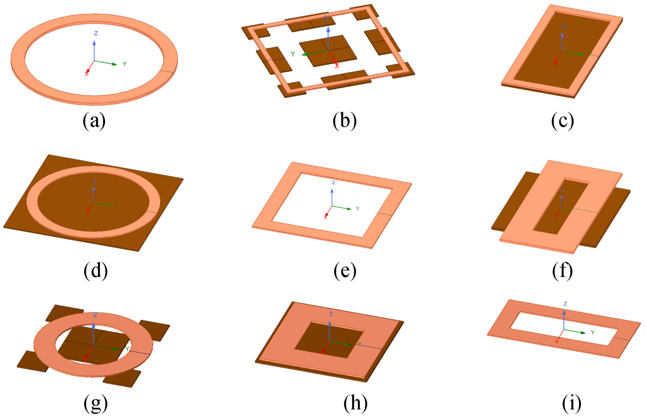
(a) (b) (c)
(d) (e) (f)
(g) (h) (i)

Fig. 3. Coils with parameters combination of the orthogonal table.

The AC resistance is related to DC resistance, skin effect resistance, proximity effect resistance, and resistance caused by core loss. So, DC resistance should be calculated and given by (9)–(12).

$$L = \sum_{i=1}^{n} \pi(D - 5 \text{ mm} * (i - 1)) \tag{9}$$

$$L = \sum_{i=1}^{n} 4(L_0 - 5 \text{ mm} * (i - 1)) \tag{10}$$

$$L = \sum_{i=1}^{n} 3(L_0 - 5 \text{ mm} * (i - 1)). \tag{11}$$

Equation (9) is for circular coils, (10) is for square coils, and (11) is for rectangular coils. L refers to the length of the Litz wire used to build the coil, and i refers to the number of turns. The DC resistance of each coil satisfies the following equation:

$$R = \rho * L/S \tag{12}$$

where ρ refers to the electrical resistivity of copper, which is 17.8 mΩ per meter when the sectional area is 1 mm^2. L refers to the length of the Litz wire obtained from (9) to (11), and S refers to the equational sectional area of the Litz wire. So, the calculated DC resistance and AC resistance of each coil are given in Table IV.

The ratio between AC resistance and DC resistance is used to reflect the impact on resistance of the parameters in the orthogonal table. Then, the F-test determines whether the parameter inflects the ratio. The result of the F-test is given in Table V.

Table V lists that only the cores distribution has a p-value less than 0.05, significantly affecting the ratio. Meanwhile, this variable is positively correlated with the ratio. As proved by other papers, the higher the magnetic flux in the ferrite core in

TABLE IV
MEASURED COIL RESISTANCE

Experiment no.	DC resistance (mΩ)	AC resistance (mΩ)
1	18.85713	24.36
2	50.20848	87.87
3	25.3207	41.3
4	75.44864	183.5
5	64.61561	112.78
6	30.556	52.17
7	70.98857	142.82
8	58.93733	128.3
9	98.23224	185.58

TABLE V
RESULT OF F-TEST

Parameter	Coefficient (95% CI)	p-value
Number of turns	(-0.06729, 0.483)	0.12
Shape of coil	(-0.1548, 0.4532)	0.28
Size of coil	(-0.3862, 0.2695)	0.69
Cores distribution	(-0.004, 0.4946)	0.05

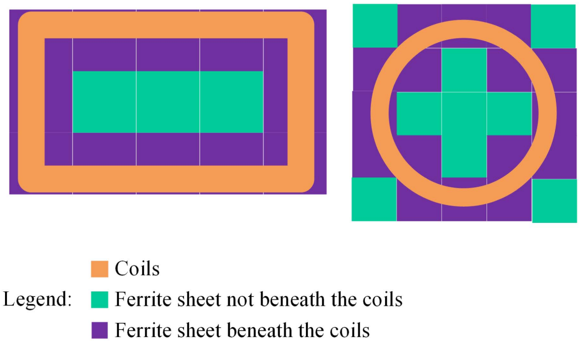

Fig. 4. Distribution of ferrite sheets.

AC excitation, the greater the core loss. So, the ferrite sheets under the coil are divided into two classes based on whether they are directly below the coil, as shown in Fig. 4.

Then, the amount of these two types of sheets in the orthogonal table is separately counted. The influence of the two types of sheets on the ratio of AC resistance to DC resistance is calculated using the multiple linear regression method. Three sets of data are added to improve accuracy. The result of multiple linear regression after excluding outliers obtains the following equation:

$$\begin{aligned} R_{\mathrm{AC}} &= (0.42a + 0.18b + 0.96)R_{\mathrm{AC0}} \\ R_{\mathrm{AC0}} &= 2.06 * R_{\mathrm{DC}} - 15.59. \end{aligned} \tag{13}$$

R_{AC} refers to the AC resistance of the coil with a ferrite coil, R_{AC0} refers to the AC resistance of the coil without a ferrite coil, and R_{DC} refers to the DC resistance of the coil according to (11)–(13). Parameter a refers to the proportion of ferrite sheets beneath the coil to the maximum number. In contrast, parameter b refers to the proportion of magnetic cores not beneath the coil to the maximum number of ferrite sheets. The maximum number of magnetic cores means the number of ferrite sheets required to fill the outer dimensions of the coil (calculated in rectangles).

The procedure of resistance estimation is as follows.

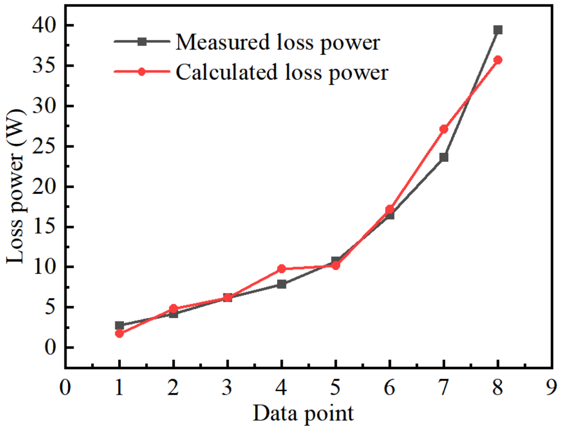

Fig. 5. Calculated and measured loss of coils in different conditions.

1) Make some coils with different numbers of turns and ferrite core distribution.
2) Calculate DC resistance using (9)–(12) and measure the AC resistance using an *LCR* meter.
3) Calculate the ratio between the AC and DC resistance.
4) Divide the cores into two types, as shown in Fig. 4.
5) Multiple linear fittings are used to calculate coefficients and complete the resistance estimation model, such as (13).

Also, the loss of coils in different conditions is analyzed. A WCS with nested coils is taken as an example. The result is shown in Fig. 5, and (5) and (6) are used to calculate the loss.

As shown in Fig. 5, the difference between the calculated and measured power loss is insignificant, and the trend is the same, further verifying the accuracy of the proposed resistance estimation model. The proposed method is more simple than the model-based methods and is more accurate than the FEA-based methods.

IV. MULTIOBJECTIVE OPTIMIZATION WITH PREFERENCES BASED ON T-NSGAII

As the exhaustive method requires a lot of time and single-objective optimization algorithms struggle to balance multiple optimization objectives, multiobjective optimization is used to balance multiple optimization objectives. However, as the number of optimization objectives increases, the density of individuals on the Pareto front will decrease, and it may not even be easy to find individuals who meet the requirements. So, the T-NSGAII combined with LHS is used to increase the density of individuals that meet the requirements, and the principle of T-NSGAII is analyzed as follows.

A. *Analysis of T-NSGAII*

NSGA-II method is a widely used multiobjective optimization. In the NSGAII method, each parameter combination is considered an individual, such as a GA. Nondominant sorting is used to achieve multiobjective optimization. Then, individuals are ranked according to their dominant relationships, and individuals at higher levels of dominance are prioritized for

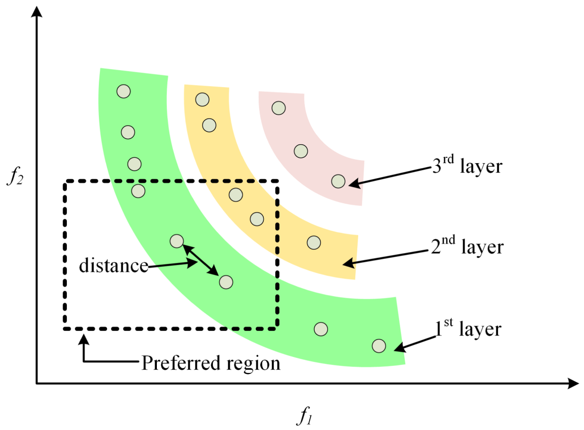

Fig. 6. Sorting layer and preferred region of T-NSGAII.

selection. Then, for individuals at the same level of dominance, those far away from other individuals will be prioritized for selection. Therefore, a uniform distribution of individuals on the Pareto front is achieved.

However, as mentioned above, the density of individuals on the Pareto front will decrease when the number of optimization objectives increases, and it is difficult to add more individuals in one generation. The T-NSGAII method is used to solve this problem, and a preference region decided by the researchers is used to restrict the individual distribution area to increase the density of individuals.

For the optimization of WCS, the preferred region can be defined as the range of mutual inductance, the range of magnetic coupler's resistance, or the range of other parameters that affect WCS performance. In this article, the aligned mutual inductance, fluctuation of mutual inductance, and resistance of the magnetic coupler are used as goals to be optimized. Also, their range is defined as the preferred region.

The individuals within the preferred region are prioritized and selected, and (14) is used to judge whether an individual is winning the preferred region

$$\forall a_i, (i_{\text{bot}} - a_i)(i_{\text{top}} - a_i) < 0 \tag{14}$$

where i_{top} and i_{bot} refer to the top and bottom limit of the preferred region of the *i*-th parameter, and a_i refers to the *i*-th parameter value of the individual.

Three methods rank the individuals and select individuals for cross and mutation. The first one is nondominated sorting, which means that if there is a dominant relationship between two individuals, they will be placed at different levels. The dominant relationship can be shown in (15) when assuming the lower parameter value is better, where *a* and *b* refer to two individuals, and a_i and b_i refer to their *i*-th parameter values.

$$\forall i \in N, a_i \leq b_i, a \succ b. \tag{15}$$

Fig. 6 shows the rank layer and preferred region of the individuals. Individuals in layer 1 have the highest priority when selecting individuals for the next iteration. The next is layer 2; layer 3 has the lowest selecting priority in the figure.

The second one is sorting based on preference regions and distance. For individuals in the same layer, those within the preferred region have higher priority. The distance between the individual and the region's center is used for the individuals out of the preferred region as follows, as shown in (16), where *dis* refers to the distance between the individual and the region's center:

$$dis = \begin{cases} -1 & \text{if } a \text{ is in the region} \\ \sqrt{\sum_{i=1}^{n} (a_i - i_{\text{cent}})^2} & \text{else} \end{cases}. \tag{16}$$

The third one is the crowding distance or the shared distance. The minimum Euler distance between individuals can be obtained for both of them, which can be obtained by (17) where *dis* refers to the Euler distance between individuals.

Crowding distance separates individuals when there are enough individuals within the preferred region. In this case, individuals far from others have a higher priority in being chosen. Shared distance separates individuals when there is no individual in the preferred area. In this case, crowding distance may drive individuals distributed throughout the entire Pareto front, which is unsuitable. So, a predefined value, or shared distance, separates individuals. The individual with a minimum Euler distance less than the shared distance has a lower priority in being chosen.

$$dis = \sqrt{\sum_{i=1}^{n} (b_i{}^2 - a_i{}^2)}. \tag{17}$$

Cross mutation generates the next generation after choosing individuals according to the above methods. In this article, linear crossover and polynomial variation are used.

In addition, LHS is chosen to generate the initial population to achieve more uniform sampling. All feasible combinations can be seen as sampling space, and each selected combination of parameters is seen as a dot. The sampling space is divided evenly into several layers based on the number of samples. Then, randomly sample each layer and ensure each layer is considered. Latin hypercube reduces the number of sampling points and the time cost of the slow FEA process.

The procedure of the optimization of WCS using the T-NSGAII method is shown as follows.

1) Initialize all algorithm parameters, including maximum iteration, current iteration, parameter *m*, etc.
2) Define preference regions, calculate the center point, and define the dispersion factor.
3) Generate the initial population of individuals using the LHS method.
4) Analyze the performance of the individuals based on FEA software and calculate their fitness based on the simulation result.
5) Nondominant sorting is used to rank and select the individuals with a higher dominant level, as shown in Fig. 6.
6) To select individuals of the lower rank, determine whether they are in the preferred region using (14) and (16) and use crowding distance or shared distance to rank individuals as shown in (17).

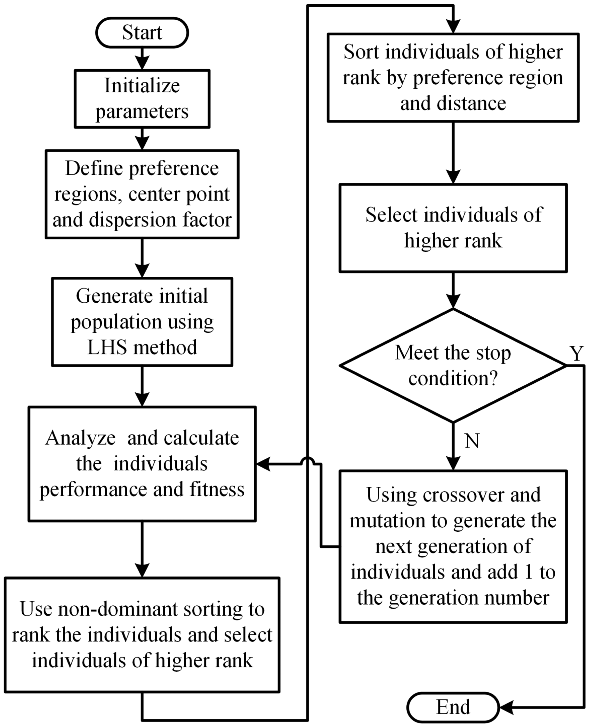

Fig. 7. Flowchart of the proposed method.

7) Select the remaining individuals based on the abovementioned methods.
8) Judge whether the stop condition is met. If the stop condition is met, stop the algorithm and output the results. Otherwise, add 1 to the number of iterations and use cross and mutation to generate the next iteration. Then, go back to step 4).

The flowchart of the proposed method is shown in Fig. 7.

For the optimization of WCS, parameters such as the number of turns, size of coils, and distribution of ferrite cores can influence the system's performance. So, these parameters can be optimized. Aligned mutual inductance and mutual inductance fluctuations caused by misalignment are widely used evaluation indicators of antimisalignment ability. As analyzed above, coil resistance has a significant impact on coil loss. So, they can be selected as goals of optimization.

B. Magnetic Coupling Structures Optimization Based on T-NSGAII

The optimization of the nested coils is taken as an example. The parameters that need to be optimized are the turns of the outer coil on the transmitter side or *N1*, the inner coil turns of the transmitter side or *N2*, the turns of the receiver side or *NR*, the transmitting distance or *H*, and the size of the receiver side or *LR*. The link between coil parameters and optimized parameters is shown in Fig. 8. Because parameters *N1*, *N2*, and *NR* are turns of coils, they should be integers, and their range is 1–19. The range of parameter *LR* is 150–230 mm, and the stepping is 10 mm, while the range of *H* is 30–70 mm, and its stepping is also 10 mm.

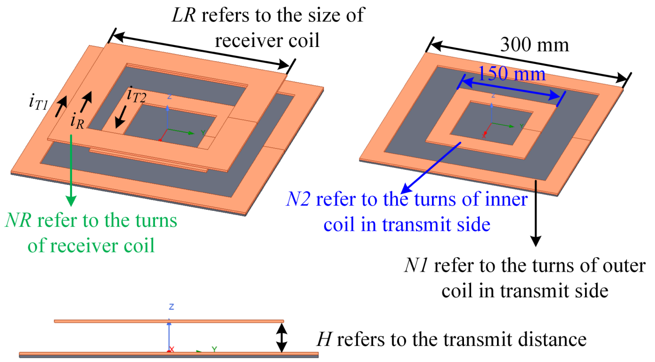

Fig. 8. Parameters of the coil need to be optimized.

When the parameters are out of range, the following strategies are used to make them within the range. If the parameters *N1*, *N2*, or *NR* are not integers, round them to the nearest integer, and if the parameter is larger than 20 or smaller than 1, a random integer between 1 and 20 is used to replace it. If the parameters *LR* and *H* are not multiples of 10, the nearest multiple of 10 is used to replace them, and if they are out of range, a random multiple of 10 within the range is used to replace it.

Three optimization goals are used. According to the analysis in Section II, the goal of mutual inductance is 19.5 μH, and mutual inductance fluctuation in the range of 120 mm is chosen as the second goal based on the characteristics of magnetic coupling structures. Equations to calculate the two goals are given as follows:

$$G_1 = \frac{M_0 - 19.5}{M_0}$$
$$G_2 = \frac{\max((M_{max} - M_0), (M_0 - M_{min}))}{M_0} \tag{18}$$

where M_0 refers to the aligned mutual inductance, and $M_{max,}$ and M_{min} refer to the range's maximum and minimum mutual inductance. As mentioned in Section II, the loss of magnetic coupling structure is positively correlated with the resistance of the transmitting and receiving coils. Therefore, the resistance of the transmitting and receiving coils is considered as one of the optimization goals. The equation used to calculate the resistance of the transmitting and receiving coils is shown in (13). As the parameters of the magnetic coupling structure are shown in Fig. 8, the length of the Litz wire is obtained as

$$LT1 = 4\sum_{i=1}^{N1}(300 - 5(i-1))$$
$$LT2 = 4\sum_{i=1}^{N2}(150 - 5(i-1))$$
$$LR1 = 4\sum_{i=1}^{NR}(L_R - 5(i-1)). \tag{19}$$

The *LT1*, *LT2*, and *LR1* are the length of the Litz wire used to make these coils. Because only the transmitting side has a ferrite core, the resistance of the magnetic coupling structure satisfies

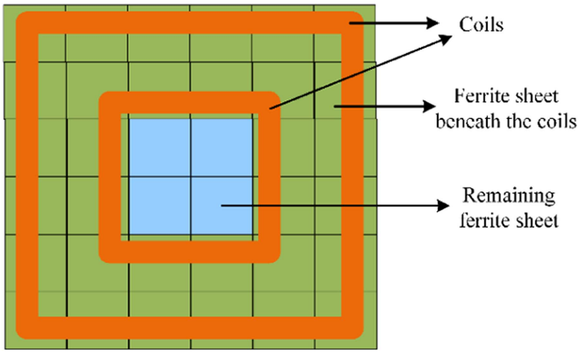

Fig. 9. Structure of the transmitter coil and the distribution of ferrite.

TABLE VI
PARAMETERS OF THE T-NSGAII ALGORITHM

Parameter	Value
Maximum number of iterations	25
Number of initial individuals	25
Number of other individuals	36
Preferred region	Cuboid, from (0, 0, 0) to (0.3, 0.25, 0.6)
Dispersion factor	0.05

(20) according to the analysis in Section III, and the structure of the transmitter coil and the distribution of ferrite are shown in Fig. 9. As shown in Fig. 9, the total number of ferrite sheets is 36 while 32 of them are beneath the coil and 4 of them are not. So, parameter a is 0.89, and parameter b is 0.11, as Section III-B mentions. According to (13), the resistance of the transmitting coil with magnetic core is increased by 35% compared to the coil without magnetic core.

$$R_{Tx} = 1.35(17.86(LT1 + LT2) - 15.59)$$
$$R_{Rx} = 17.86LR - 15.59$$
$$G_3 = R_{Tx} + R_{Rx}. \tag{20}$$

The preferred region of aligned mutual inductance, or G_1, is set to less than 0.3, and the region of mutual inductance fluctuation, or G_2, is set to less than 0.25. The preferred region of resistance of the coupler, or G_3, is set to less than 0.6 to increase the efficiency. Other parameters of the algorithm are given in Table VI, and the number of initial individuals is set to 25 to simplify the LHS progress.

When the algorithm meets the end condition, some individuals in the preferred region are given in Table VII, and the bolded and italic individual is chosen for the experiment. The definitions of parameters are shown in Fig. 8.

The fitness of the individuals is shown in Fig. 10, and the preferred region is shown in the blue cube. As the figure shows, individuals become increasingly concentrated within their preferred region as the algorithm progresses and are evenly distributed within the region.

TABLE VII
SOME OUTPUT RESULTS OF THE T-NSGAII ALGORITHM

Number	Parameters					Goals		
	H	LR	N1	N2	NR	G_1	G_2	G_3
1	30	220	8	4	17	0.29	0.22	0.42
2	30	220	8	4	19	0.29	0.18	0.44
3	***30***	***230***	***11***	***11***	***15***	***0.14***	***0.16***	***0.56***
4	30	220	12	13	14	0.3	0.06	0.57
5	40	220	10	6	19	0.15	0.2	0.51

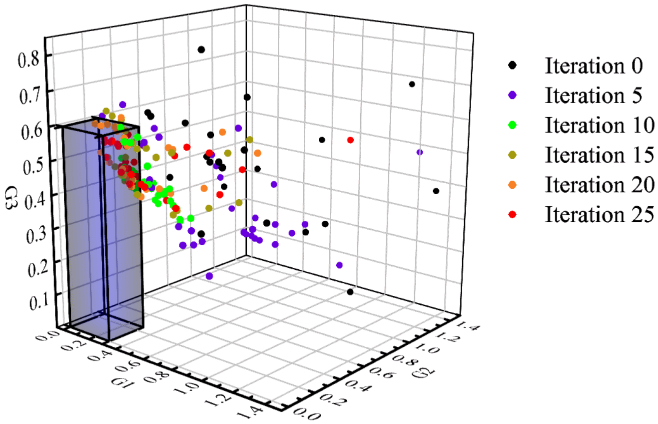

Fig. 10. Fitness of the individuals as the algorithm progresses.

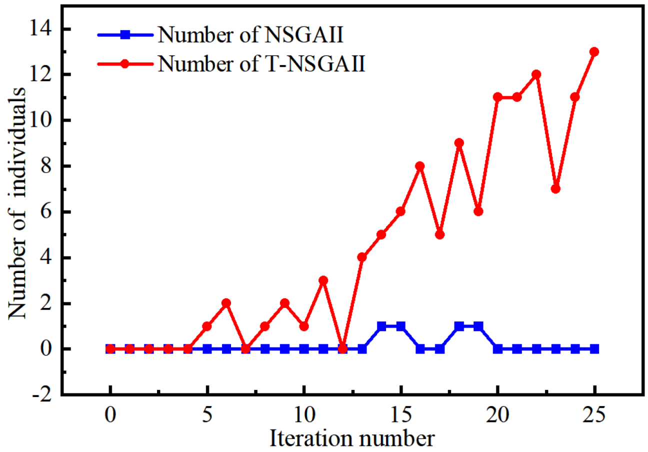

Fig. 11. Number of individuals in the preferred region of the two algorithms.

The traditional NSGAII method is used to optimize the same coil for comparison. Parameters of both methods are set to the same, including number of individuals, probability of crossover and mutation, and maximum number of Iterations. When the algorithm meets the end condition, the number of individuals in the preferred region of the two algorithms is shown in Fig. 11, where the red line shows the number of T-NSGAII while the blue line shows the number of NSGAII.

As shown in Fig. 11, although the traditional NSGAII algorithm has good convergence performance, most individuals are out of the preferred region. Instead, they concentrated on the Pareto front and distributed evenly. Some of the individual outputs of the two methods are given in Table VIII. In the table, coils 1 and 2 are output by the T-NSGAII method, while coils

TABLE VIII
Some Individual Outputs of the Two Methods

	H	L2	N1	N2	NR	G1	G2	G3
Coil1	30	230	11	11	15	0.14	0.16	0.56
Coil2	30	220	12	13	14	0.3	0.06	0.57
Coil3	30	230	6	1	20	0.01	0.45	0.37
Coil4	40	200	15	14	13	0.29	0.14	0.62
Coil5	30	200	8	2	16	0.29	0.34	0.36

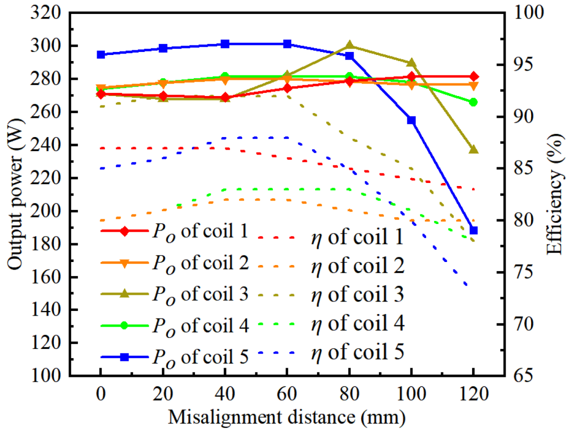

Fig. 12. Output power and efficiency of the coils.

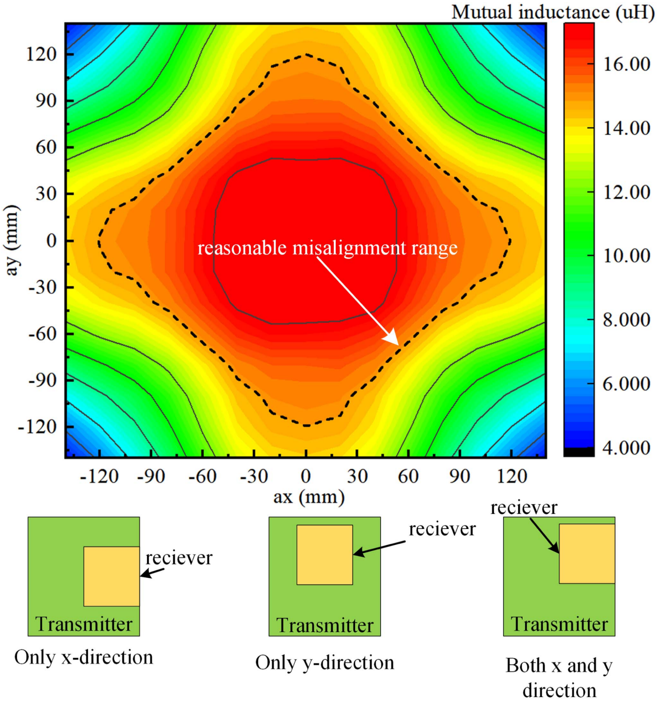

Fig. 13. Mutual induce when misalignment occurs with reasonable misalignment range.

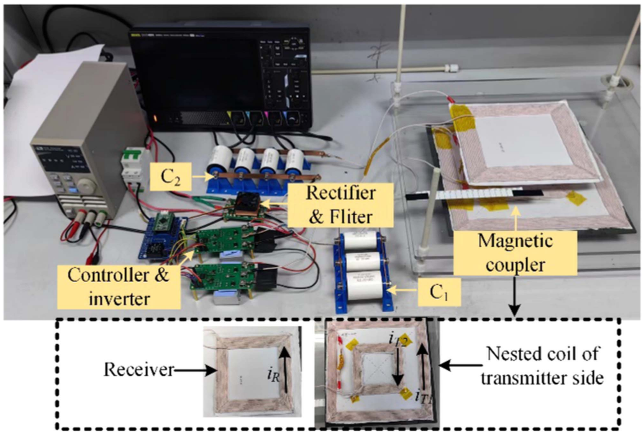

Fig. 14. Experimental setup of the designed system.

3–5 are output by the traditional NSGAII method, and G1–G3 refers to the optimization goals.

As given in Table VIII, coils 3–5 have different preferences, which is also a characteristic of the NSGAII method. However, none of them are in the preferred region. On the other hand, coils 1 and 2 have a more balanced performance, and both are in the preferred region, which is a characteristic of the proposed T-NSGAII method. When misalignment occurs, the above coils' simulated output power and efficiency are shown in Fig. 12, where P_o refers to the output power and η refers to the efficiency.

As shown in Fig. 12, coil 1 has minor power fluctuation and has higher efficiency, with the highest efficiency when the misalignment distance is 120 mm. Although coil 2 has the slightest power fluctuation, the efficiency is less than coil 1. Although coils 3 and 5 have high aligned efficiency, they quickly decrease when misalignment occurs, mainly because of their large mutual inductance fluctuation. Coil 4 also has slight power fluctuation, but the efficiency is low because the resistance is large and aligned mutual inductance is low.

So, coil 1 is selected for experimental verification, and its mutual inducement when misalignment occurs with a reasonable misalignment range is shown in Fig. 13. The area enclosed by the black dashed line is a reasonable range of misalignment. It reaches 40% of the size of the transmitting end in both the *x* and *y* directions.

According to the result of the optimization experiment, the T-NSGAII method is considered an algorithm that can increase individual density within preference regions without increasing computational complexity. More individuals in the preference region are achieved compared to the traditional NSGAII algorithm, and much less computation is achieved compared with the enumeration method. The proposed method only requires 900 datasets to generate enough individuals within the preference area. Compared to the 200 000 sets required by the exhaustive method, the T-NSGAII method has achieved optimization with only 0.45% of data.

V. Experimental Verification

A. Experimental Setup

A 300 W experimental setup of a WCS with nonresonant SS compensation that operates at an open-loop state is shown in Fig. 14. Note that this setup mainly validates the feasibility and the optimization result. The control system can be added based on actual needs. The transmitting side contains an inverter with

TABLE IX
SYSTEM PARAMETERS OF AN EXPERIMENTAL PROTOTYPE

Symbol	Parameter note	Value
U_{bus}	System DC bus voltage	50 V
f	Working frequency	85 kHz
L_1	Transmitter coil inductance	142.6 μH
R_1	Transmitter coil resistance	345.9 mΩ
C1	Compensation capacitance of the transmitter	25 nF
L_2	Receiver coil inductance	96.7 μH
R_2	Receiver coil resistance	190.7 mΩ
C2	Compensation capacitance of the receiver	36 nF
M	Mutual inductance	17.67 μH

TABLE X
MEASURED AND CALCULATED RESISTANCE OF THE NESTED COIL

Parameter	Measured (mΩ)	Calculated (mΩ)	Error (%)
R_1	345.9	370.95	7.2
R_2	190.7	188.97	0.9
R_{sum}	536.6	559.92	4.3

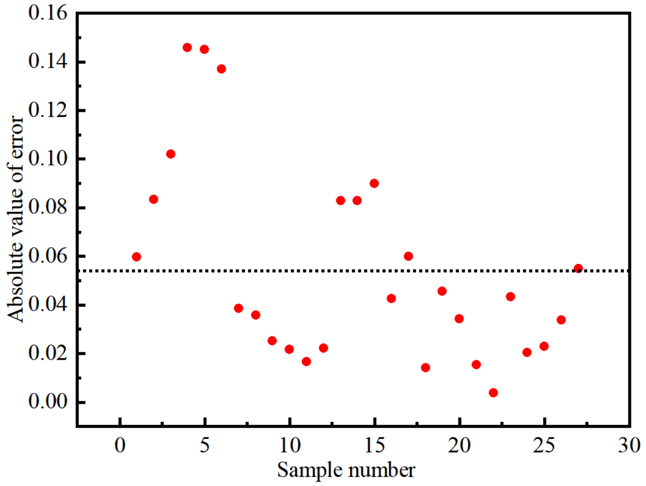

Fig. 15. Error absolute value of different coils.

four MOSFETs (STW48N65DM2) and a driver chip (EG2113S). The receiver side contains a rectifier, including four diodes (NTSB40120CTG) with low forward voltage.

All of the coils are made by Litz wire with a diameter of 2.5 mm, and the compensation topology includes two sets of nonpolar capacitors. Thin film capacitors are used to increase current capacity. The ferrite core is made of a PC95 ferrite sheet, and the sheet size is 53 mm∗53 mm∗2.5 mm. The DC power supply and DC electronic load used to test the output performance of the designed WCS are IT6526C and IT8524B+, manufactured by ITECH. The main system parameters are listed in Table IX.

B. Experimental Results Analysis

The resistance of nested coils is also calculated using (20). Its error is given in Table X , where R_1 refers to the resistance of the transmitting coil, R_2 refers to the resistance of the receiver coil, and R_{sum} refers to the sum of the above two, similar to the optimization result given in Table VII. Then, the resistance of

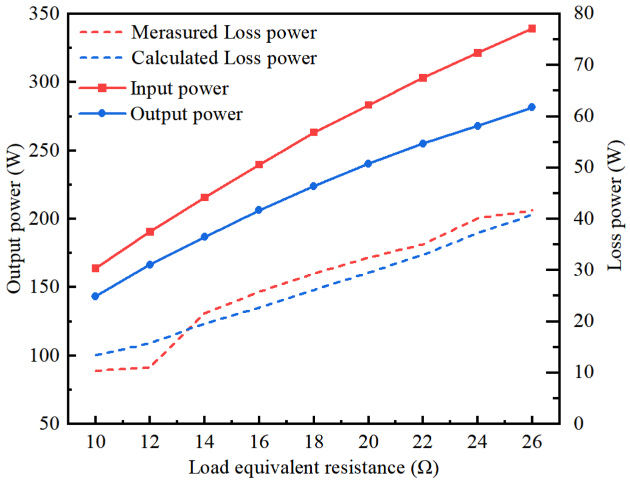

Fig. 16. Experimental results of loss.

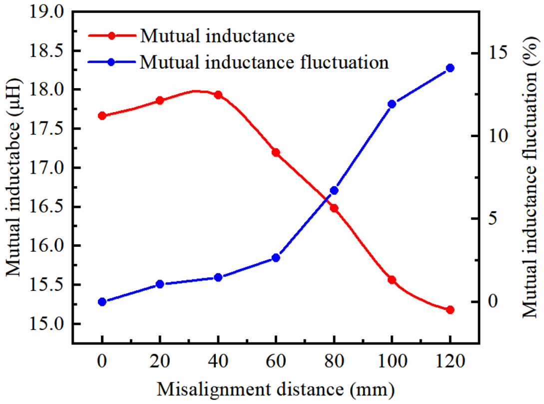

Fig. 17. Experimental results of mutual inductance versus misalignment distance.

The absolute value of the error is shown in Fig. 15. The average error is about 5.04%, as indicated by the black dashed line, and the maximum error value is about 14%.

Also, the loss of the magnetic coupler with nested coils under different loads is measured and calculated by (5) and (6). The results are shown in Fig. 16 . As the figure shows, the measured AC loss is close to the calculated result and has similar trends, indicating that the proposed resistance calculation method applies to the estimation of different coil resistances and losses.

Combined with the horizontal misalignment range shown in Fig. 13, Fig. 17 shows the measured mutual inductance of the magnetic coupler. Because of the symmetry of the magnetic coupling structure, its mutual inductance exhibits similar behavior in the *x* and *y* directions. Therefore, the impact caused by the misalignment in the *x* direction was tested. VC4092E LCR meter made by Victor is used to measure the self-inductance in Table X, and the mutual inductance can be obtained based on (21), following the steps below:

1) Measure the self-inductance of the transmitting and receiving coil separately and denote them as L_1 and L_2, respectively.
2) Short-circuit the receiving coil, measure the self-inductance of the transmitting coil currently, and denote

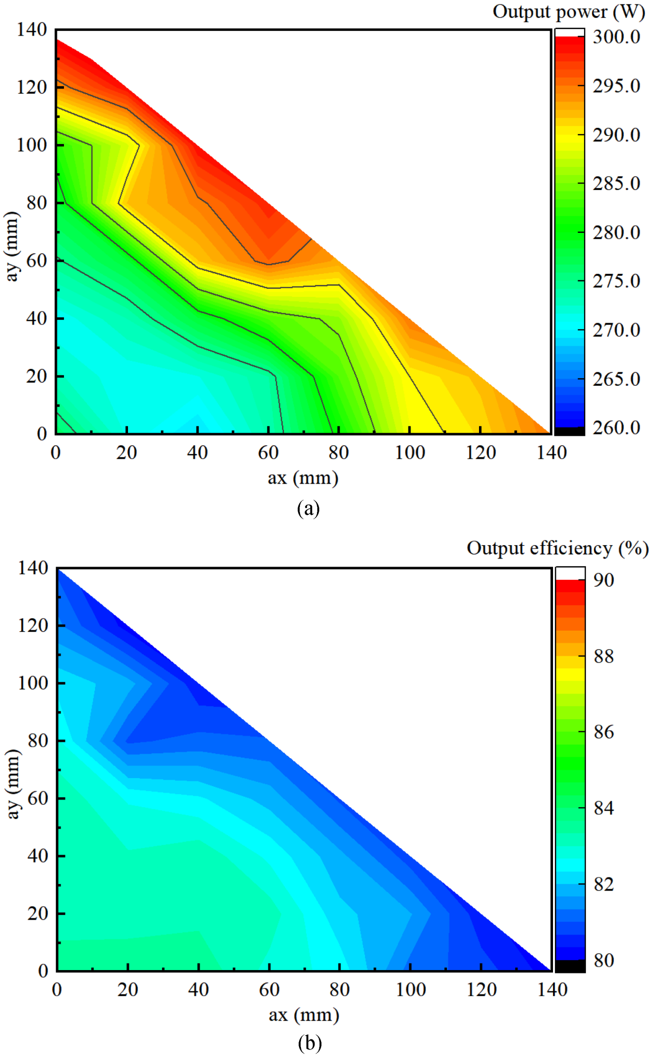

(a)

(b)

Fig. 18. Experimental results of output power and efficiency.

3) Calculate the mutual inductance using the following equation:

$$M = \sqrt{(L_1 - L_{1s})L_2}. \tag{21}$$

The measured mutual inductance and its fluctuation are shown in Fig. 17. The fluctuation of mutual inductance is about 15% when the misalignment distance is 120 mm, which is 40% of the size of the transmitter. Also, it is similar to the result of simulation.

Fig. 18 shows the output power and efficiency under the misalignment when the load is 25 Ω. Due to the symmetry of the magnetic coupling structure, it has similar antimisalignment characteristics in all four quadrants. The maximum output power fluctuation is about 5% and maintained the efficiency of more than 80% in the range of 120 mm, similar to the result shown in Figs. 12 and 13.

Fig. 19 shows the output power and its fluctuations of resonant and nonresonant systems. The output power fluctuation of the nonresonant system is much lower than the resonant one, similar to the result shown in Fig. 2.

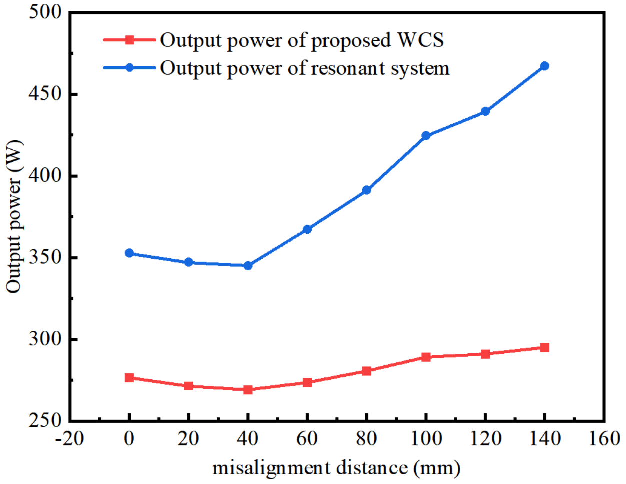

Fig. 19. Experimental results of output power.

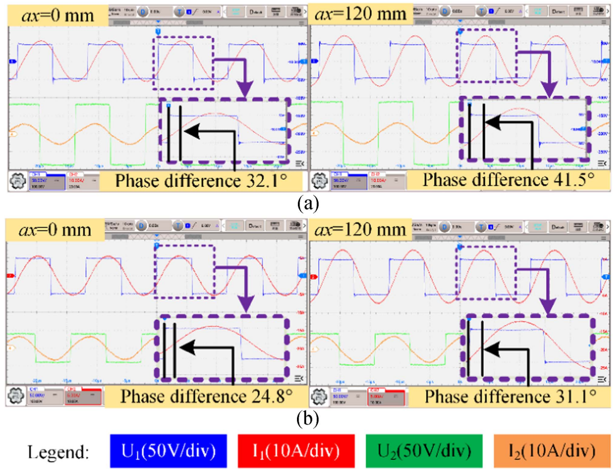

Fig. 20. Experimental waveforms when $ax = 0$ mm and 120 mm. (a) $R_o = 25\ \Omega$. (b) $R_o = 10\ \Omega$.

The result also shows the optimized nonresonant WCS's antimisalignment ability, and the system's waveform is shown in Fig. 20, showing the nonresonant characteristics and antimisalignment ability of the optimized WCS.

Closed-loop experiments were used to verify the applicability of the optimized WCS. After adding the necessary sensors and controllers, the system achieved CC/CV charging, and the output waveform is shown in Fig. 21, which shows the fast response and slight overshoot when the load changes. Moreover, Fig. 21 also shows the nonresonant characteristics of the system.

Although the accuracy of the proposed resistance estimation is limited by the accuracy of measuring the resistance of a given coil, the accuracy of shape, and the accuracy of power measuring, the simulation and experimental results are consistent, and the error in resistance estimation is relatively small, proving the applicability of the proposed resistance estimation method. The proposed optimization method can also increase individual density within the preferred region without increasing computational cost. The optimized nonresonant WCS can achieve antimisalignment ability under specific loads.

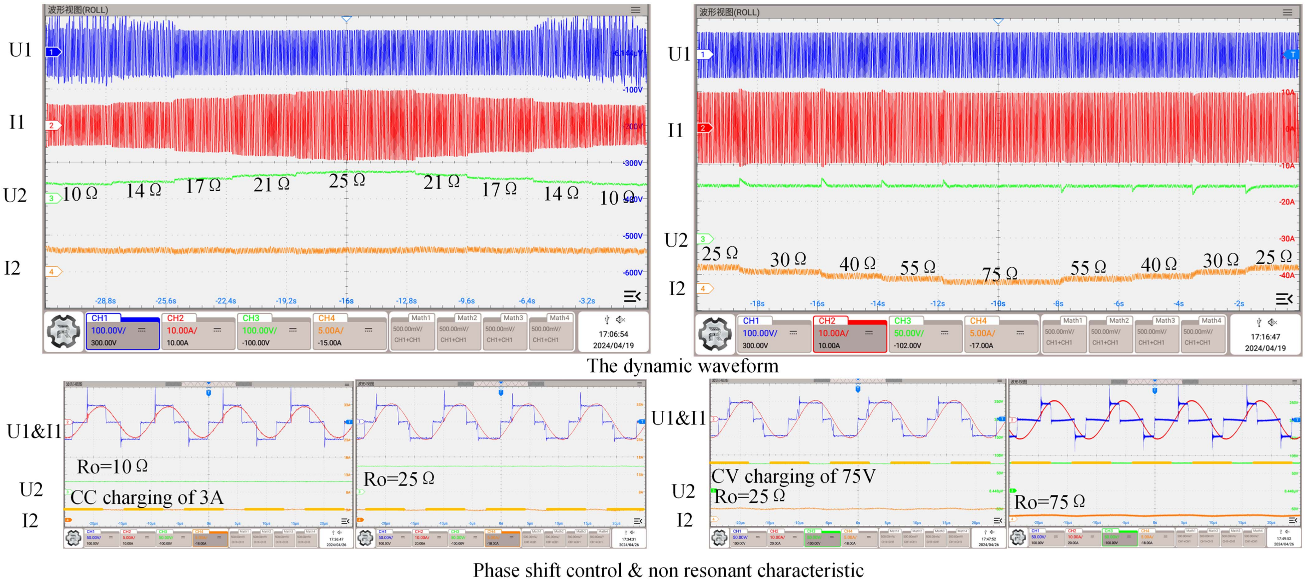

(a) (b)

Fig. 21. Dynamic experimental waveforms. (a) CC charging of 3 A, (b) CV charging of 75 V.

Also, the proposed resistance estimation and optimization methods can be applied to other systems, such as different coil shapes and resonant systems. Finally, it should be noted that selecting a preference region may require experience, and expanding the optimization method's applicability is our future work.

VI. CONCLUSION

This article proposed a method for estimating the resistance of coils with magnetic cores, which was used to analyze the losses of WCS compensated by nonresonant SS. The working principle of nonresonant SS-compensated WCS was analyzed, and its antimisalignment ability was also analyzed. Meanwhile, a preference-based multiobjective optimization algorithm (T-NSGAII) was proposed to optimize WCS. The multiobjective optimization of nested coils was used as an example. The resistance model was established as one of the optimization objectives, combined with the positive mutual inductance and antimisalignment ability to obtain the optimization goal. Then, preference-based multiobjective optimization of the magnetic coupler was obtained, and one group was selected for experimental verification. The results show that under a load resistance of 25 Ω, when the misalignment distance is less than 40% of the transmitter's width, the output power fluctuation is less than 5%, and the efficiency can be maintained at over 80%.

REFERENCES

[1] Y. Zhang et al., "Misalignment-tolerant dual-transmitter electric vehicle wireless charging system with reconfigurable topologies," *IEEE Trans. Power Electron.*, vol. 37, no. 8, pp. 8816–8819, Aug. 2022.

[2] P. Cao et al., "Embedded lightweight squirrel-cage receiver coil for drone misalignment-tolerant wireless charging," *IEEE Trans. Power Electron.*, vol. 38, no. 3, pp. 2884–2888, Mar. 2023.

[3] K. Chen, Y. Ouyang, X. Yang, N. C. Cheung, E. K.-W. Cheng, and J. Pan, "A high-interoperability optimal frequency control method for the AGV dynamic wireless charging systems without communication," *IEEE Trans. Power Electron.*, vol. 39, no. 3, pp. 3797–3808, Mar. 2024.

[4] G. Wei, X. Jin, C. Wang, J. Feng, C. Zhu, and M. I. Matveevich, "An automatic coil design method with modified AC resistance evaluation for achieving maximum coil–coil efficiency WPT systems," *IEEE Trans. Power Electron.*, vol. 35, no. 6, pp. 6114–6126, Jun. 2020.

[5] T. Noda, T. Nagashima, X. Wei, M. K. Kazimierczuk, and H. Sekiya, "Design procedure for wireless power transfer system with inductive coupling-coil optimizations using PSO," in *Proc. IEEE Int. Symp. Circuits Syst.*, 2016, pp. 646–649.

[6] G. Chen, D. Hu, and S. Chien, "Optimizing battery-electric-feeder service and wireless charging locations with nested genetic algorithm," *IEEE Access*, vol. 8, pp. 67166–67178, 2020.

[7] J. H. Lee, J.-W. Kim, J.-Y. Song, D.-W. Kim, Y.-J. Kim, and S.-Y. Jung, "Distance-based intelligent particle swarm optimization for optimal design of permanent magnet synchronous machine," *IEEE Trans. Magn.*, vol. 53, no. 6, Jun. 2017, Art. no. 7206804.

[8] C. Xing, T. Liu, J. Zhao, and Y. Lin, "Parameter identification of primary side wireless charging system based on adaptive particle swarm optimization," in *Proc. 37th Chin. Control Conf.*, 2018, pp. 1667–1671.

[9] Y. Yang, S.-C. Tan, and S. Y. R. Hui, "Front-end parameter monitoring method based on two-layer adaptive differential evolution for SS-compensated wireless power transfer systems," *IEEE Trans. Ind. Inform.*, vol. 15, no. 11, pp. 6101–6113, Nov. 2019.

[10] H. Liu et al., "Anti-misalignment capability optimization for laminated magnetic couplers in wireless charging systems using balanced particle swarm optimization method," *J. Power Electron.*, vol. 23, no. 2, pp. 345–354, 2023.

[11] Y. Ye and K. W. E. Cheng, "Analysis and optimization of switched capacitor power conversion circuits with parasitic resistances and inductances," *IEEE Trans. Power Electron.*, vol. 32, no. 3, pp. 2018–2028, Mar. 2017.

[12] A. A. S. Mohamed, S. An, and O. Mohammed, "Coil design optimization of power pad in IPT system for electric vehicle applications," *IEEE Trans. Magn.*, vol. 54, no. 4, Apr. 2018, Art. no. 9300405.

[13] K. Sun, J. Wang, R. Burgos, and D. Boroyevich, "Design and multi-objective optimization of coil and magnetic for wireless power transfer in auxiliary power network," in *Proc. IEEE Appl. Power Electron. Conf. Expo.*, 2020, pp. 819–824.

[14] Z. Li, J. He, Y. Huo, M. Ban, Y. Liu, and J. Liu, "High-misalignment tolerance and output adjustable wireless charging system via detuned series–series compensated reconfigurable transmission channels," *IEEE Trans. Power Electron.*, vol. 38, no. 10, pp. 11786–11801, Oct. 2023.

[15] J. Ma, Z. Li, Y. Liu, M. Ban, and W. Song, "Thermal analysis and optimization of the magnetic coupler for wireless charging system," *IEEE Trans. Power Electron.*, vol. 38, no. 12, pp. 16269–16280, Dec. 2023.

[16] T. Yilmaz, N. Hasan, R. Zane, and Z. Pantic, “Multi-objective optimization of circular magnetic couplers for wireless power transfer applications,” *IEEE Trans. Magn.*, vol. 53, no. 8, Aug. 2017, Art. no. 8700312.

[17] J. Molina, L. V. Santana, A. G. Hernández-Díaz, and C. A. C. Coello, “g-dominance: Reference point based dominance for multi-objective metaheuristics,” *Eur. J. Oper. Res.*, vol. 197, no. 2, pp. 685–692, Sep. 2009.

[18] K. Deb and A. Kumar, “Light beam search based multi-objective optimization using evolutionary algorithms,” in *Proc. IEEE Congr. Evol. Comput.*, 2007, pp. 2125–2132.

[19] H. Trautmann and J. Mehnen, “Preference-based Pareto optimization in certain and noisy environments,” *Eng. Optim.*, vol. 41, no. 1, pp. 23–38, Dec. 2008.

[20] J. Szlapczynska and R. Szlapczynski, “Preference-based evolutionary multi-objective optimization in ship weather routing,” *Appl. Soft Comput.*, vol. 84, no. 1, Nov. 2008, Art. no. 105742.

[21] K.-S. Yoon, S.-H. Lee, I.-K. Cho, H.-J. Lee, and G.-H. Cho, “Dual receiver coils wireless power transfer system with interleaving switching,” *IEEE Trans. Power Electron.*, vol. 33, no. 12, pp. 10016–10020, Dec. 2018.

[22] J. Liu, Q. Deng, D. Czarkowski, M. K. Kazimierczuk, H. Zhou, and W. Hu, “Frequency optimization for inductive power transfer based on AC resistance evaluation in litz-wire coil,” *IEEE Trans. Power Electron.*, vol. 34, no. 3, pp. 2355–2363, Mar. 2019.

[23] M. Wu et al., “Modeling of litz-wire DD coil with ferrite core for wireless power transfer system,” *IEEE Trans. Power Electron.*, vol. 38, no. 5, pp. 6653–6669, May 2023.

[24] A. Abramovitz and S. Ben-Yaakov, “RGSE-based SPICE model of ferrite core losses,” *IEEE Trans. Power Electron.*, vol. 33, no. 4, pp. 2825–2831, Apr. 2018.

[25] S. Barg, K. Ammous, H. Mejbri, and A. Ammous, “An improved empirical formulation for magnetic core losses estimation under nonsinusoidal induction,” *IEEE Trans. Power Electron.*, vol. 32, no. 3, pp. 2146–2154, Mar. 2017.

[26] Z. Yan, Z. Weibo, and T. Guanghui, “A core loss calculation method for DC/DC power converters based on sinusoidal losses,” *IEEE Trans. Power Electron.*, vol. 38, no. 1, pp. 692–702, Jan. 2023.

[27] C.-H. Lee, S.-T. Ho, S.-H. Hsu, and J.-A. Jiang, “Taguchi-based design of planar circular coils used wireless charging of mobile phones,” *IEEE Trans. Consum. Electron.*, vol. 70, no. 1, pp. 299–307, Feb. 2024.

[28] Z. Li, H. Liu, Y. Huo, J. He, Y. Tian, and J. Liu, “High-misalignment tolerance wireless charging system for constant power output using dual transmission channels with magnetic flux controlled inductors,” *IEEE Trans. Power Electron.*, vol. 37, no. 11, pp. 13930–13945, Nov. 2022.

Hao Liu was born in Linhe, Inner Mongolia Autonomous Region, China, in 1997. He received the B.S. degree in electrical engineering and automation from the Harbin Institute of Technology, Harbin, China, in 2019, and the M.S. degree in control science and engineering from Northeast Forestry University, Harbin, China, in 2023. He is currently working toward the Ph.D. degree in electrical engineering with Zhejiang University, Hangzhou, China.

His current research interests include power electronics and electromagnetic compatibility.

Zhenjie Li (Member, IEEE) received the B.S. degree in measurement and control technology and instruments from the School of Measurement and Control Technology and Communication Engineering, Harbin University of Science and Technology, Harbin, China, in 2012, the M.S. degree in instrument science and technology, and the Ph.D. degree in electrical engineering from the School of Electrical Engineering and Automation, Harbin Institute of Technology, Harbin, China, in 2014 and 2020, respectively.

Since 2020, he has been an Associate Professor with the College of Computer and Control Engineering, Northeast Forestry University, Harbin, China. He has published a highly cited ESI paper in the IEEE TRANSACTIONS ON POWER ELECTRONICS. His research interests include designing and controlling the wireless charging system with multiple applications and power levels.

Henglin Chen was born in Ji’an, Jiangxi, China, in 1979. He received the B.S. and M.S. degrees in material science and engineering from Tianjin University, Tianjin, China, in 2000 and 2003, respectively, and the Ph.D. degree in electrical engineering from Zhejiang University, Hangzhou, China, in 2007.

Since 2008, he has been with the College of Electrical Engineering, Zhejiang University, where he was a Postdoctoral Researcher between 2008 and 2009, and was a Lecturer between 2009 and 2011. He was promoted to Associate Professor in 2011. From 2011 to 2012, he was a Visiting Scholar with Clemson University, Clemson, SC, USA. He has authored or coauthored more than 80 papers published in international journals and conference proceedings. His main research interests include power electronics and electromagnetic compatibility.

Dr. Chen was the recipient of the Delta Visiting Scholar Award from Delta Environmental and Educational Foundation in 2010, the Young Scientist Award from the IEEE Asia-Pacific Electromagnetic Compatibility in 2016, and the Best Paper Award from the 13th IEEE Vehicle Power and Propulsion Conference in 2016. He was the Chair of the Smart Grid and Low Frequency Electromagnetic Compatibility in the 2022 Asia-Pasic International Symposium on Electromagnetic Compatibility and Technical Exhibition, the Chair of the Topical Symposium on Smart Grid and Power Electronics EMC in the 2018 Joint IEEE Electromagnetic Compatibility and Asia-Pasic International Symposium on Electromagnetic Compatibility and Technical Exhibition, the Session Chair in the 2017 Asia-Pacific Electromagnetic Week Conference on Electromagnetic Compatibility, the Chair of the Special Session on EMC Issues in Electric Vehicles in the 2016 IEEE VPPC Conference, and the Chair of the Topical Symposium on Smart Grid and Power Electronics EMC in the 2016 Asia-Pasic International Symposium on Electromagnetic Compatibility and Technical Exhibition.